# Kent Academic Repository

## Full text document (pdf)

## Citation for published version

Chin, Catherine and Bradu, Adrian and Lim, Rongxuan and Khandwala, Mona and Schofield, John and Leick, Lasse and Podoleanu, Adrian G.H. (2016) Master/slave optical coherence tomography imaging of eyelid basal cell carcinoma. Applied Optics, 55 (26). pp. 7378-7386. ISSN 1559-128X.

## DOI

https://doi.org/10.1364/AO.55.007378

## Link to record in KAR

http://kar.kent.ac.uk/57409/

## Document Version

Author's Accepted Manuscript

# Master/slave optical coherence tomography imaging of eyelid basal cell carcinoma

Catherine Chin,[1,3,*] Adrian Bradu,[1] Rongxuan Lim,[2] Mona Khandwala,[2] John Schofield,[1,2] Lasse Leick,[3] and Adrian Podoleanu[1]

[1]Applied Optics Group, University of Kent, Canterbury CT2 7NH, UK
[2]Maidstone and Tunbridge Wells NHS Trust Hospital, Maidstone ME16 9QQ, UK
[3]NKT Photonics A/S, Blokken 84, Birkerød, DK-3460, Denmark
*Corresponding author: cc539@kent.ac.uk

Optical coherence tomography (OCT) is fast emerging as an additional non-interventional modality for skin tumor detection and diagnosis. A master/slave flying spot OCT configuration was assembled to detect periocular basal cell carcinomas (BCC). A swept source at 1300 nm and sweeping speed of 50 kHz were used. A three-step process was involved. First, 384 channeled spectra using a mirror were stored for 384 optical path differences at the master stage. Then, the stored channeled spectra (masks) were correlated with the channeled spectrum from the BCC tissue to produce 384 en face OCT images (200 × 200 pixels) for the optical path difference values used to acquire the masks. Finally, these en face slices were stacked to form a volume to cross-reference BCC tumor margins in the orthogonal plane. Per each eyelid sample, several en face images of 200 × 200 lateral pixels are produced in the time to scan laterally a complete raster of 1.6 s. Combination of the en face views with the cross-sectioning views allow for better discrimination of BCCs comparable to using cross-sectional imaging alone, as previously reported using the conventional fast-Fourier-transform–based OCT techniques.     © 2016 Optical Society of America

## 1. INTRODUCTION

Basal cell carcinoma (BCC) is the most common form of skin cancer in Caucasians [1] and accounts for 80%–90% of all eyelid malignancies [2,3]. It is estimated that there are 53,000 new BCC cases diagnosed in the UK yearly [4]. The gold standard for tumor diagnosis involves surgical biopsy for histological analysis [5]. To reduce patient morbidity from surgery, non-invasive methods of diagnosis and determining tumor margins have been investigated in recent years. They include reflectance confocal microscopy (RCM) [6], high frequency ultrasound (HFUS) [7], multispectral imaging [8], multiphoton microscopy [9], the fluorescent technique [10], confocal scanning laser microscopy (CSLM) [11], and optical coherence tomography (OCT) [12,13]. Although these technologies provide valuable information, they are not yet widely adopted by mainstream health care professionals to provide the high level of certainty essential for accurate treatment. None of these emerging techniques have been used solely on their own or proved to be superior to the gold standard. These new techniques are often used to bridge the gap of limitation on established technologies, demanding new imaging systems with better penetration depth

and sensitivity. Nevertheless, recent literature has suggested that OCT in *en face* imaging mode presents the potential for improved diagnostic specificity of BCC morphology compared with clinical assessment and dermoscopy alone [14,15].

For this reason, we have developed an *en face* optical coherence tomography (OCT) system powered with our enhanced master/slave (MS) technique [16]. Compared to conventional fast Fourier transform (FFT)-based OCT, the MS technique is tolerant to the non-uniformities in the modulation frequency of the spectra acquired, as well as to dispersion in the interferometer [17]. Therefore, the MS technique allows achievement of the theoretical expected parameters for the sensitivity and for the axial resolution as determined by the bandwidth of the system and by the spectral domain principle. The MS technique leads to attainment of such values with no need for resampling of data. In conventional FFT-based OCT, the axial resolution and sensitivity are as good as the resampling/data linearization methods, which generally operate well at shallow depths only. Additionally, the MS technique gives direct access to information from selected depths, allowing the real-time display of one or more *en face* OCT images from such depths [18]. The MS method has been applied to OCT imaging of the eye fundus,

and by harnessing the power of graphic cards, real-time production of *en face* images was made possible [19].

This is a pilot study aiming to correlate the histological features of periocular BCC to features seen on the OCT scan using the MS technique. To the best of our knowledge, this is the first pilot study using the master/slave OCT technique for imaging periocular BCCs. Prior to this, three other studies to image BCC were conducted by our group using dual-wavelength (840 and 1300 nm) time domain (TD)-OCT [20], FFT-based OCT [21], and dynamic focus (DF)-OCT [22]. Based on the experience we gathered from these three tests, we identified that it is essential in performing accurate correlations with histology data to acquire high-resolution OCT images and correctly identify the margins of any skin lesion precisely. On the wavelength selection, we identified that light at 1300 nm suffers less scattering in tissue, thus providing better signal strength compared to 850 nm when used for imaging BCC [19–23].

Independent to our group's research, the use of 1300 nm for OCT imaging was further documented by the study of BCC that employs a combined RCM/OCT system for *ex vivo* imaging [24]. The data processing of OCT signals is based on the conventional FFT-based technique. In contrast to the MS technique, dispersion compensation and interpolation are employed. The resulting set of 512 OCT raster images, using their method, could be acquired in 13 s. While the RCM channel delivers *en face* images, the OCT is performed in cross section. Single *en face* images are inferred by software cut of volumes of A-scans and are placed in comparison with the RCM images.

Another study employed a commercial 20 kHz tunable laser to produce 120 stack OCT images of size 6 mm × 6 mm in between 10–20 s [25].

None of the OCT systems referenced above are capable of producing *en face* images in real time.

The use of high-definition OCT as an auxiliary diagnostic tool to histology has received an overwhelming positive response by clinicians, as evidenced by a study that looked into the effectiveness of locating BCC with OCT. This was compared to histology analysis involving both experienced and inexperienced dermatologists [26]. We drew inspiration from these state-of-the-art research studies in developing our master/slave OCT system, with an aim to offer simplified, more robust image display in a shorter time.

## 2. METHODS AND MATERIALS

### A. Master/Slave OCT

The schematic diagram of the MS-OCT system assembled is shown in Fig. 1. Light is emitted from a swept source (SS) operating at 1310 nm central wavelength with a 100 nm sweeping range, 50 kHz sweeping speed, and 15 mW output power (model SSOCT-1310, Axsun Technology, Massachusetts, USA). An interferometer, using two directional couplers DC1 and DC2, was assembled. The light from the source enters the first directional coupler (DC1, model FOBC-2-1310-20, AFW Technology, Australia) with a splitting ratio of 80:20. One output delivers 80% of light intensity into the reference arm, and 20% of light into the object arm.
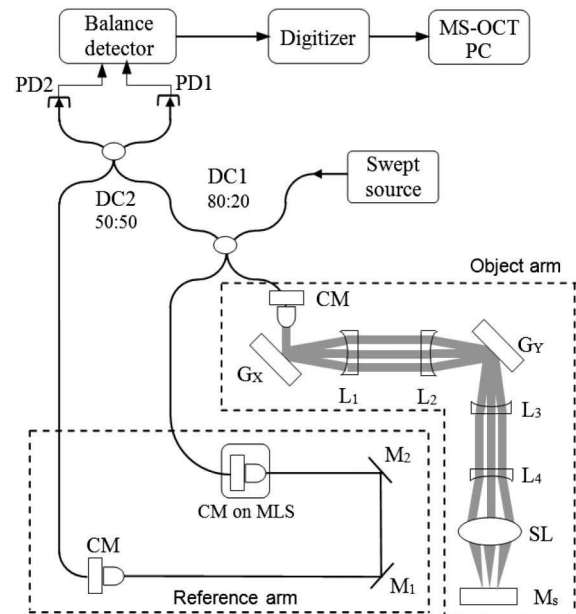


**Fig. 1.** OCT system configuration ($G_X$, $G_Y$, galvo scanners; $L_1$, $L_2$, $L_3$, $L_4$, lenses; SL, scan lens; $M_1$, $M_2$, mirrors; CM, free-space to fiber coupler; MLS, motorized linear stage; DC, directional coupler; PD1, PD2, InGaAs photodiodes; $M_s$, mirror used at the master stage, to be replaced with the BCC specimen at the Slave stage).

In the object arm, the interface optics includes an achromatic lens (CM) to collimate the output beam of the fiber, four lenses for beam expansion (L1-L4, $f = 75$ mm, AC-127-030-C, Thorlabs), and a scan lens (SL). The SL is an OCT-optimized microscope objective (LSM03, 5×, Thorlabs). For a 4 mm beam diameter incident on the SL, transversal resolution of the spot on the sample is 15 μm. The transversal resolution obtained was verified by imaging a USAF 1951 resolution target. Two galvo-scanners are installed in the object arm, denoted as $G_X$ (frame) and $G_Y$ (line) in Fig. 1.

Both $G_X$ and $G_Y$ are driven with triangular ramps. Since SS has a tuning frequency of 50 kHz, each of the 200 lateral pixels are acquired within 20 μs. $G_X$ is driven with a triangular signal, where each ramp duration is 20 μs/pixel × 200 pixels = 4 ms, with every other ramp discarded, so at a frequency of 125 Hz. The frame scanner $G_Y$ is driven with a triangular signal, which for 200 lines requires 1.6 s. With a measured transversal resolution of 15 μm, the lateral image size is limited to 3 mm × 3 mm. A single ramp of the frame signal is used for data acquisition, while the other ramp is used for data transfer to the GPU and data processing. As a result, the time needed to acquire each 2D *en face* dataset of 200 × 200 = 40,000 channeled spectra is 1.6 s.

The light into the reference arm is reflected off a set of mirrors (M1, M2), then into the second directional coupler (DC2, model FOBC-2-1310-50, AFW Technology, Australia), where it is combined with the signal from the object arm to produce interference patterns. The outputs of the DC2 are connected to the photodetectors PD1 and PD2 of a balance photodetector module (model BPD-200, Santec, Japan, 200 MHz). This

signal is sent to a digitizer (Alazartech, Canada, model ATS9350, 500 MB/s). This is embedded into a PC with an Intel Xeon processor (model E5646, 2.4 GHz, 6 cores) and a GPU card (GeForce GTX 780 Ti), loaded with a custom 64-bit LabVIEW 2014 program to display simultaneously *en face* images from 40 different depths [28,29].

The imaging process using the master/slave (MS) method is a two-step process. First, at the master stage, a mirror ($M_S$) is placed in lieu of the BCC specimen in the focal plane of SL. A set of 384 channeled spectra (masks), are collected and stored. The masks are acquired for MLS positions separated by 10 μm steps using a motorized translation stage, MLS (model MFA-CC, repeatability 0.3 μm, speed 2.5 mm/s, Newport) driven by a motion controller (ESP301, Newport). These masks represent the channeled spectra at the OCT interferometer output for 384 values obtained by equivalently displacing the mirror $M_S$ by 5 μm. Thus, with 384 masks, an axial depth range of 1.8 mm in air is achieved.

A special program was created to allow quick acquisition of masks by shifting the MLS to a new incremented position by the chosen differential interval (10 μm), followed by time to wait for mechanical vibrations to settle and then followed by the storage of mask for that position, then moved to the next position, and so on. The whole process takes less than 5 min and once masks are collected, the process does not need to be repeated. Collection of masks is performed with no voltage applied to the two galvo-scanners, i.e., using the optical beam on-axis.

The second stage (slave) involves imaging the BCC specimen that replaces the mirror $M_S$. Each BCC specimen is positioned in front of the SL. 384 *en face* images are obtained by correlating the 384 masks with the acquired channeled spectra of the BCC tissue, but a reduced number of such images is displayed, in this case 40. Figure 2 shows a typical screen of the raster displayed by the MS technique. Three categories of images are simultaneously presented and they are refreshed simultaneously: (a) *en face* OCT images at 40 simultaneous depths, (b) two cross-sectional images, and (c) a compound image to help with guidance, made from the average of the 40 *en face* images displayed. The *en face* OCT images and the compound image have 200 pixels × 200 pixels while the cross-sectional OCT images have 200 pixels lateral and 384 pixels in depth (along the vertical axis, equal to the number of masks). The differential distance between the numbers of *en face* images displayed, as well as the depth of the first *en face* images in the left corner, can be adjusted with cursors on-screen (not shown, but similar to the procedure detailed in [28]).

The compound display was found useful in adjusting the relative position of the specimens in front of the scan lens SL. Here this uses the 40 images displayed; however, this can be modified to use any number in any order of the 398 *en face* images generated by the end of each scanning frame.

Each category of images is produced using a special program developed in CUDA. The simultaneous display of the three categories of images takes advantage of methods developed in previous reports [22,29], to speed up the processing of comparison operation at the core of the MS technique to the level where it can compete with the FFT-based OCT method, while maintaining the other MS advantages (tolerance to dispersion and tuning nonlinearities with implications in achieving high axial resolution and better sensitivity).
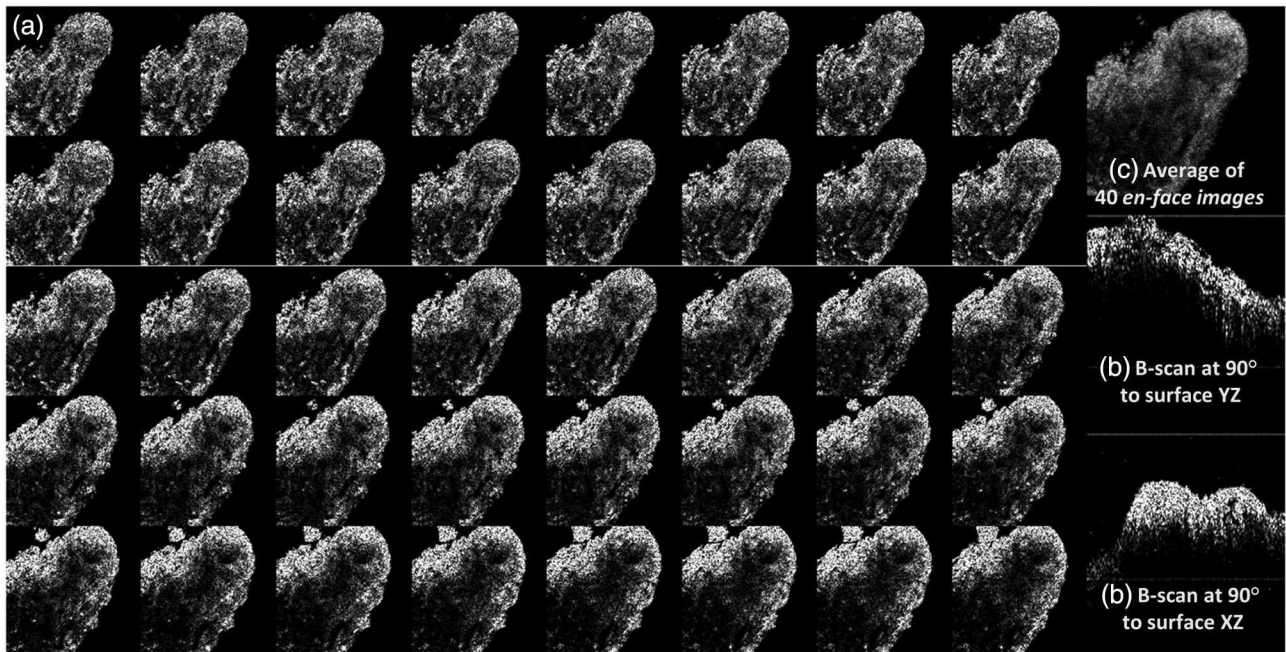


**Fig. 2.** Illustration of master/slave raster made from 3 categories of images. (a) 40 *en face* OCT images separated axially by 5 μm (measured in air), (b) two cross-sectional OCT images acquired from two orthogonal orientations, and (c) an average of the *en face* images displayed for guidance. The horizontal size of all images and the vertical size of *en face* OCT images: 3 mm × 3 mm. The vertical size of the two cross-sectional images is 3 mm × 1.5 mm (measured in air). The *en face* images have 200 pixels × 200 pixels while the cross-sectional images 200 pixels × 300 pixels.
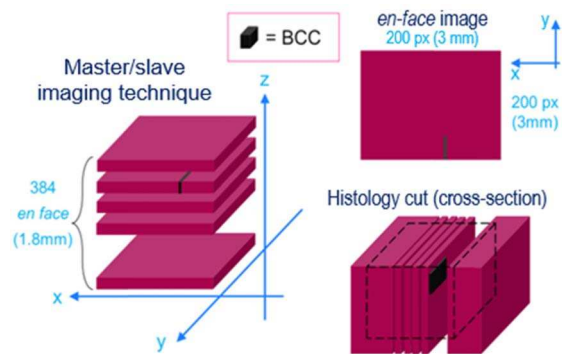
F3:1    **Fig. 3.**    Illustration of assembling cross-sectional scans from *en face*
F3:2    images. *En face* images are delivered by the MS-OCT technique.

215    The axial resolution of the system is determined by the
216    tuning bandwidth of the optical source. With a SS of
217    $\Delta\lambda = 100$ nm bandwidth, we can expect an axial resolution
218    of around 7.5 µm.
219    Histology data are collected in the cross-section plane; there-
220    fore, to compare and correlate suspected BCC features side by
221    side, we need to prepare such cuts from the *en face* images
222    produced by the MS technique. Therefore, for subsequent
223    analysis, the *en face* slices acquired are stacked to form a 3D
224    volume. A slice was cut orthogonally to the *en face* surface
225    to produce a cross-sectional OCT image, as shown in Fig. 3.

226    **B. Tissue Imaging**
227    Three consecutive patients over the age of 18 with a biopsy-
228    proven periocular nodular BCC, without previous eyelid sur-
229    gery, were enrolled into the study. The study protocol was
230    approved by the Research and Development Department of
231    the Maidstone and Tunbridge Wells NHS Trust and also
232    by the Ethics Committee at the School of Physical Sciences,
233    University of Kent. Informed consent was obtained from the
234    participants.
235    All BCC lesions were surgically excised with predetermined
236    2 mm margins of normal skin. The orientation of each speci-
237    men was specified by using 6/0 silk sutures of various lengths to
238    mark 3 of the margins of the lesion. The excised specimens
239    were placed in 10% neutral buffered formalin and transported
240    from Maidstone Hospital to the University of Kent within 3 h

241    of excision for OCT imaging. For purpose of image acquisition,
242    the BCC tissue was placed on a transparent microscope glass
243    slice, with its superior margin aligned to the horizontal direc-
244    tion of the optical beam axis at the microscope focus of the
245    OCT machine. After OCT imaging was completed, the spec-
246    imens were placed back into 10% neutral buffered formalin
247    and transported to the Maidstone Hospital Histology
248    Department the same day.

**C. Histology Analysis**
250    The specimens were allowed to fix in 10% neutral buffered
251    formalin for 24 h and then "bread sliced" at 2 mm intervals
252    at 90 deg to the skin surface, retaining orientation as
253    denoted by the marking sutures. Each slice was processed
254    and paraffin-embedded with serial sections cut at 2 µm inter-
255    vals, then mounted on glass slides stained with haematoxylin
256    and eosin, and viewed in a conventional light microscope.
257    Photomicrographs were captured for comparison with OCT
258    images and correlation undertaken by identification of the
259    matching features of the OCT and histology images under
260    supervision of two of the authors (JS and CC).

**3. RESULTS**
262    The three separate excised BCC specimen biopsy tissues from
263    the three patients were imaged using the MS-OCT system.
264    Each sample has been marked Case 1, Case 2, and Case 3,
265    respectively. To allow comparison to histology data, we as-
266    sembled the *en face* images into a 3D volume. A cross-sectional
267    OCT image was then sliced orthogonally to the volume surface.
268    Using this method, 200 cross-sectional images were recon-
269    structed at different lateral positions. We ran our algorithm
270    through all these images from the center of the sample to locate
271    possible BCC features contained within each of the cross-sec-
272    tional images. Diagnosis of BCC via OCT correlation requires
273    demarcation of tumor margins to determine BCC invasion,
274    and visual interpretation of morphological features as reported
275    in pathology-to-OCT correlation studies [30–33].
276    Histology images of Case 1 using an Olympus BX50 micro-
277    scope are shown in Fig. 4. The haematoxyphilic (purple) areas
278    equate to lobules and strands of BCC. The eosinophilic (pink)
279    areas are supporting stroma and normal dermis. The corre-
280    sponding OCT cross sections are shown in Fig. 5. The areas
281    containing BCCs are compared against the marked area in
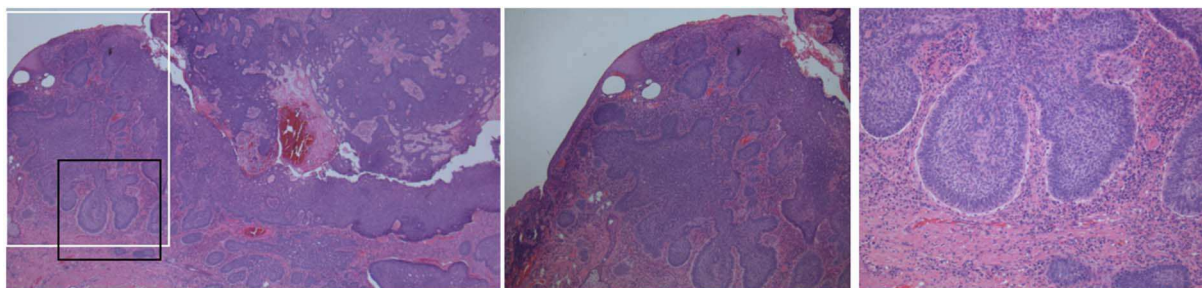


F4:1    **Fig. 4.**    Histology images of the nodular BCC corresponding to tissue sample of Case 1. The images show tumor lobules that correspond to
F4:2    honeycomb structures. The lateral size × depth size of left image is 5 mm × 3 mm. The middle image shows an enlarged view of the white boxed
F4:3    region in the left image. The right image shows an enlarged view of the black box area in the left image. Magnification: left ×10, middle ×20, and
F4:4    right ×100.
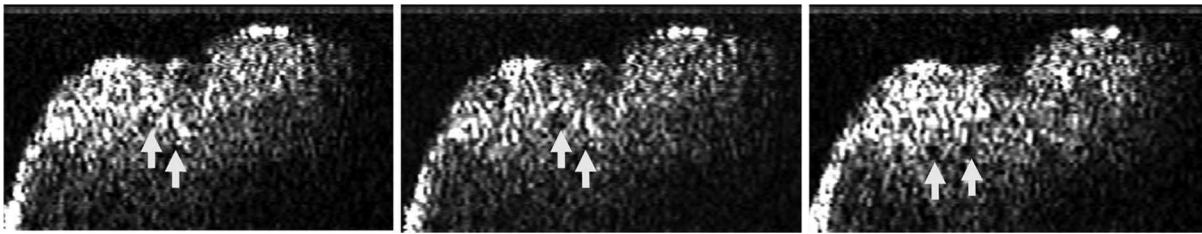
F5:1    **Fig. 5.**    Results of Case 1. Cross-sectional OCT images of eyelid BCC taken from three consecutive transverse slices at the center of the sample.
F5:2    The left, middle, and right slices are each separated by 15 μm. The size of the image is 1.2 mm × 0.8 mm. The arrows show the suspected areas
F5:3    of BCC.
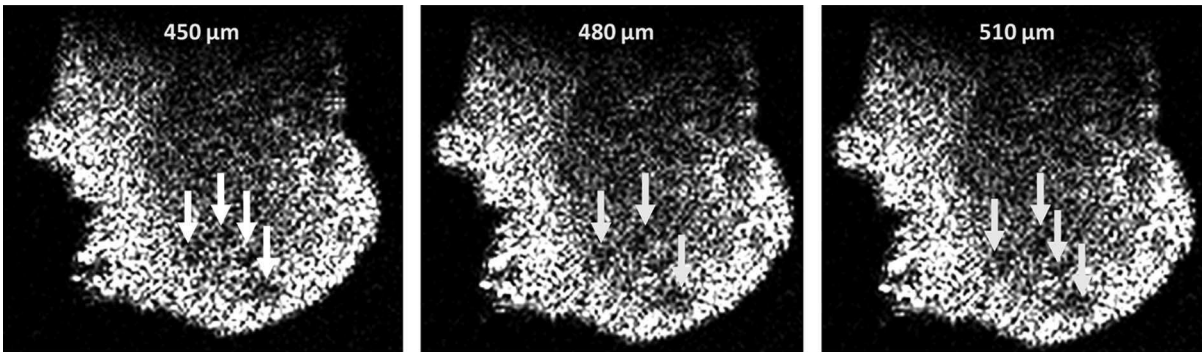


F6:1    **Fig. 6.**    Results of Case 1. *En face* OCT images of eyelid BCC taken at different depths. The depth was measured from the top of the sample in
F6:2    air. The lateral size of the image is 1.5 mm × 1.5 mm. The arrows show the areas of BCC correlated with histology data.

the histology image. *En face* images taken at 30 μm axial interval from each other (measured in air), showing features at depths of 450, 480, and 510 μm from the top of the sample are shown in Fig. 6. The corresponding BCC areas are noticeable with several dark spots surrounded by bright regions.

A more extensive type of BCC was spotted from another region of Case 1 as shown in Fig. 7. The tumors spread around in a non-uniformed pattern surrounded by healthy tissue. In the *en face* image, noticeable patterns of uneven dark stretches indicate the presence of tumor. One definite indicator of BCC in OCT images is the reduction of signal intensity.
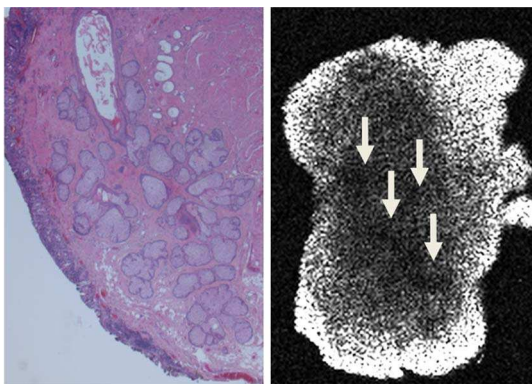


F7:1    **Fig. 7.**    Results for another region of Case 1. (Left): histology image
F7:2    showing blocks of BCC tumors. (Right): *en face* OCT image of
F7:3    corresponding region taken at a depth of 780 μm from top of sample
F7:4    (measured in air).

The presence of BCC in the *en face* images in Figs. 5, 6, and 7 is manifested in clusters of signal-free dark spots, rather than in continuous bounded areas, primarily due to the position of BCC tumor spreads across multiple axial layers of *en face* images.

The second experiment was carried out using samples of Case 2. Clinical microscopy images are shown in Fig. 8. The purple areas are identified as BCC by the histologist. Cross-sectional and *en face* images taken from this case with features associated with BCC are shown in Figs. 9 and 10. Various features are detected in the cross-sectional OCT images in Fig. 9: (1) sweat ducts identified by a consistent shallow shaft, (2) cross-sectional blood capillary showed up as a highly reflective circle, and (3) suspected BCC tumors with irregular reflectivity contrasts. Other features suspected to be BCC in OCT images (detected by an early report using time-domain OCT with dynamic focus [22]) can also be seen in images generated using the MS-OCT. These features are noticeable in Fig. 10 with scattered high-reflectivity areas that exhibit size enlargement as we move deeper into depth. BCC tissues are usually highly reflective at 1300 nm, leading to dark scattered margins surrounded by low-reflectivity tissue. The tissue areas that are lacking these random dark patches are identified as healthy tissue.

An immediate practical advantage of *en face* imaging is showing the direction in which tumors metastasize. With each *en face* image displaying the area of BCC in the transverse plane in constant intensity, less complicated analysis is required to identify the tumors, compared to measuring the reduction
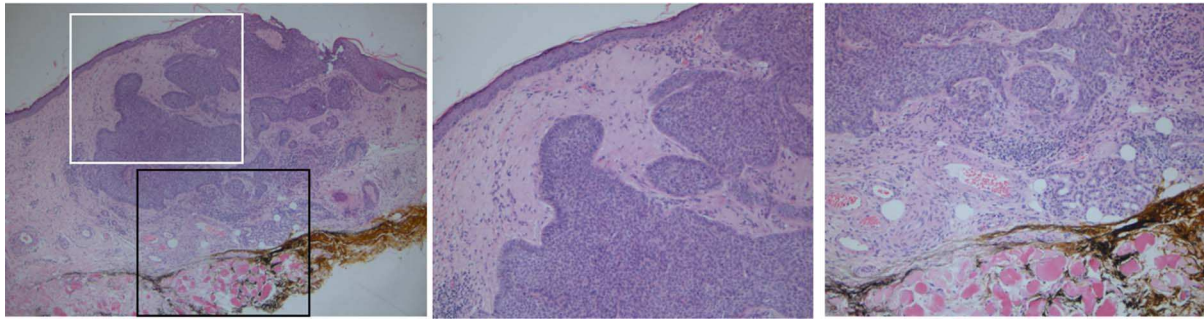
F8:1 **Fig. 8.** Histology images of superficial BCC from tissue sample of Case 2. The image on the left shows a tumor exhibiting nested and budding
F8:2 patterns. The lateral size × depth size of the left image is 4 mm × 3 mm. The middle image is an enlarged view of the white boxed region in the left
F8:3 image. The right image is an enlarged view of the black box area in the left image. Magnification: left ×20, middle ×50, and right ×50.
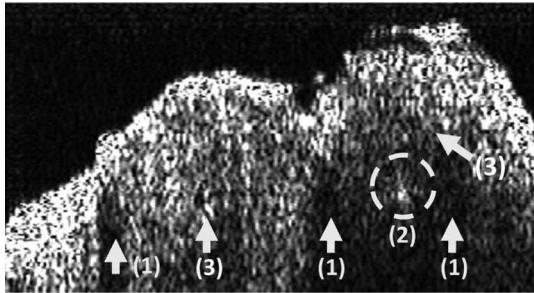


F9:1 **Fig. 9.** Results of Case 2. Cross-sectional OCT images of eyelid
F9:2 BCC taken from the center of tumor. (1) Sweat ducts. (2) Blood capil-
F9:3 lary under the dermis layer. (3) Suspected areas of BCC. The lateral
F9:4 size × depth size of image is 1.5 mm × 0.6 mm.

322 of signal strengths in the cross-sectional OCT images. This fea-
323 ture is particularly important to determine the lateral borders of
324 a BCC tumor adjacent to healthy tissue.
325     The MS-OCT ability to detect the pigmented type of BCC
326 is further evidenced in Case 3. Histology images in Fig. 11
327 show tumor lobules concentrated in pigment surrounded by
328 healthy tissue. Due to the high reflectivity of BCC, the higher
329 concentration of tumor cells blocked light transmission in the
330 tissue, producing a signal-free dark spot in the middle of the
331 cross-sectional OCT image as evidenced by arrows in Fig. 12.
332     This region can be further verified by scanning through dif-
333 ferent layers of the *en face* images in Fig. 13. As we move further
334 in depth, more common features pointing to potential BCC

335 start to unfold. OCT images are placed side by side with his-
336 tology images where correlation of tumor features was per-
337 formed. In Fig. 11, the depth data from *en face* images are
338 in agreement with the histology data that show structures of
339 BCC at approximately 0.5 mm underneath the dermis. *En face*
340 images in Figs. 6, 10, and 13 are in their original form, free
341 from any quality adjustment. In the slightly pixelated cross-sec-
342 tional OCT images of Figs. 5, 9, and 12, predominant tumor-
343 like features remain easily recognizable. Studies have shown
344 that image post-processing methods, such as spatial com-
345 pounding and de-convolution algorithms, can be used to re-
346 duce speckle and enhance signal-to-noise ratio in the
347 acquired multilayer images [34,35].

## 4. COMMENTS ON TECHNOLOGY
348

349 Based on previous experiments to characterize BCC employing
350 OCT systems at two different wavelengths, 830 and 1300 nm,
351 we have concluded that 1300 nm was better suited for imaging
352 eyelid skin tissue [20]. MS-OCT is an improvement on the
353 technique used in two previous setups, using SS-OCT [21]
354 and DF- OCT [22].
355     The MS-OCT technique proved successful in detecting com-
356 plex morphological features of skin in all three specimens im-
357 aged. Several skin features that were observed using the DF-
358 OCT technique [35] are also present in the MS-OCT *en face*
359 images. These are: (1) nodular structure of abnormal tissue,
360 (2) superficial structure of scattered tumor margins, and (3) cross
361 section of blood vessels, sweat ducts, and sweat glands in the
362 upper dermis.
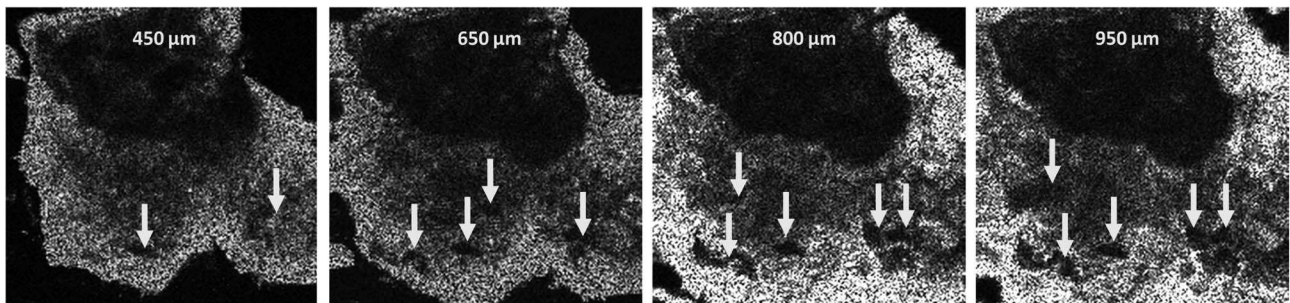


F10:1 **Fig. 10.** Results of Case 2. *En face* OCT images of eyelid BCC taken at different depths of 450–950 μm. The depth was measured from the top of
F10:2 sample in air. The arrows show the areas of BCC correlated with histology data. The size of the image is 1.5 mm × 1.5 mm.
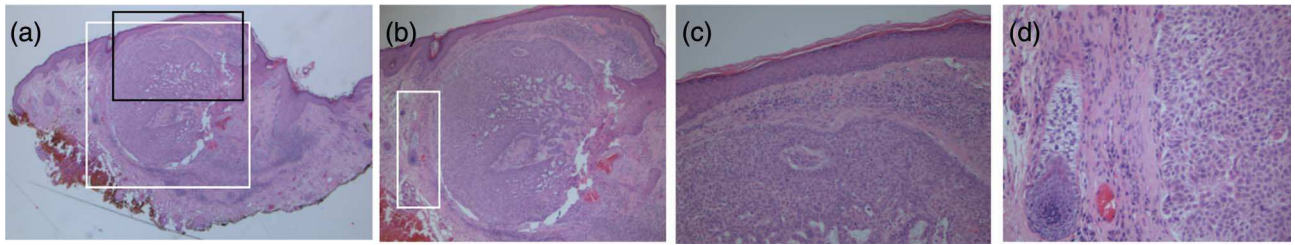
F11:1    **Fig. 11.**    Histology images of Case 3. Image in (b) shows an enlarged view of the white boxed region in image (a). Image (c) shows an enlarged view
F11:2    of the black box area of image (a). The image (d) shows an enlarged region of image (b) indicating presence of nodular-pigmented-type BCC tumor
F11:3    lobules beneath the epidermis. Magnification: (a) ×20, (b) ×50, (c) ×100, (d) ×200.
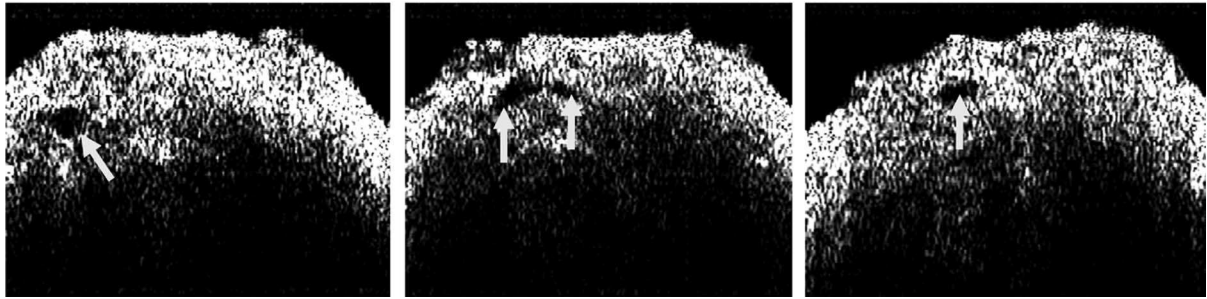


F12:1    **Fig. 12.**    Results of Case 3. Cross-sectional OCT images of suspected BCC taken at three lateral positions from the center of sample. The arrows
F12:2    show the areas with pigment correlated with histology images. The lateral size × depth size of the image is 1.5 mm × 0.6 mm.
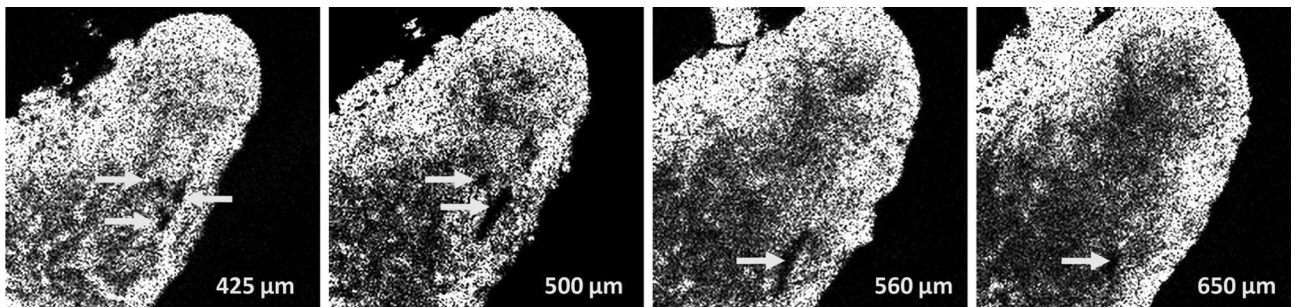


F13:1    **Fig. 13.**    Results of Case 3. *En face* OCT images of eyelid BCC taken at different depths in the range 425–650 μm. The depth was measured from
F13:2    the top of the sample in air. The arrows show the areas of BCC. The size of the image is 1.5 mm × 1.5 mm.

363    BCCs in cross-sectional OCT images can be identified by
364 three main phenomena: (a) abnormal reflectivity profile as we
365 go in depth, (b) obscure regions with clear margins, and
366 (c) repetitive inhomogeneous features different from the sur-
367 rounding cells. Similar morphological features are also used
368 to identify potential BCC candidates in the *en face* images.
369 A side-by-side comparison with histology images for all three
370 cases further validates the use of these criteria in OCT images
371 with high certainty to locate and detect various types of BCC.
372    In the first two BCC structures, nodal and superficial, the
373 presence of BCC tissue in *en face* image can be determined
374 from the absence of back reflected signal in a bounded area with
375 clear edges. The presence of some random, low-reflectivity
376 black spots indicate distribution of pigmented BCC structures.
377 The lack of signal from BCC structures can be explained by
378 higher absorption due to their denser structure compared to

normal tissue [20,21]. This feature is predominantly visible    379
on OCT systems operating at 1300 nm than on systems using    380
shorter wavelengths.    381
   Conventionally, averaging multiple *en face* images usually    382
improves the signal to noise, allowing better location of    383
BCCs otherwise unnoticeable in a cross-sectional OCT image,    384
but this is done on the expense of axial resolution.    385
   The master/slave method can equally be applied to broad-    386
band sources, by using a spectrometer, in order to achieve better    387
axial resolution [37].    388

## 5. CONCLUSIONS    389

In this pilot study, *en face* images of BCC samples taken from    390
three patients were produced using the novel master/slave    391
method. In all cases, the suspected BCC regions showed sig-    392

nificant reduction in the signal strengths compared to uniform signal reflectivity in neighboring tissues. In some cases, the presence of potential BCC can be identified by irregular scattering of high reflectivity dark spots (Fig. 6) and inconsistent light distribution pattern (Fig. 7) in skin tomograms.

All features associated with BCC demonstrated in our three previous studies [20–22] are also seen with *en face* images obtained using MS-OCT. Three common types of BCC were identified and fitted well with histology criteria. In particular, nodular BCC are noted with their low reflectivity of light at 1310 nm, closely corresponding to BCC on correlation by the histologist following standard laboratory processing. Other subtypes of BCC may also be picked up by their irregular reflectivity profile in *en face* images. High accuracy in distinguishing uncertain tumor lesions from healthy skins was established [15].

A further study has been planned once a portable handheld probe incorporating master/slave technique is manufactured. This will ease the transport of technology for clinical trials at hospitals, allowing imaging to be carried out in real time, in three possible scenarios, involving both *in-vitro* and *in-vivo* experiments: (1) pre-surgery diagnosis, (2) intra-operative assessment of precise tumor margins, (3) post-surgical side-by-side histology assessment. *In-vivo* OCT imaging would be preferred for its enhanced clinical value to dermatologists and pathologists [37–39], as the water content and skin optical properties are preserved. We acknowledge possible signal distortions due to *in-vitro* imaging.

The use of the MS-OCT technique has allowed *en face* images to display noticeable BCC features in real time. With no further image processing required, rapid assessment of BCC extent and surgical margins in excised skin specimens can be carried out, allowing for enhanced management of patients in the clinical setting.

This is a preliminary study to assess the values of the *en face* display in diagnosing BCC. The MS technique is ideally suited to deliver such display as the image is assembled directly while laterally scanning with no need to wait for a whole assembly of A-scans to be subsequently cut.

## REFERENCES

1. A. Lomas, J. Leonardi-Bee, and F. Bath-Hextall, "A systematic review of worldwide incidence of nonmelanoma skin cancer," Br. J. Dermatol. **166**, 1069–1080 (2012).
2. C. E. Margo and K. Waltz, "Basal cell carcinoma of the eyelid and periocular skin," Surv. Ophthalmol. **38**, 169–192 (1993).
3. G. W. Jung, A. I. Metelitsa, D. C. Dover, and T. G. Salopek, "Trends in incidence of nonmelanoma skin cancers in Alberta, Canada, 1988-2007," Br. J. Dermatol. **163**, 146–154 (2010).
4. F. Bath-Hextall, J. Leonardi-Bee, C. Smith, A. Meal, and R. Hubbard, "Trends in incidence of skin basal cell carcinoma. Additional evidence from a UK primary care database study," Int. J. Cancer **121**, 2105–2108 (1993).
5. (NICE Guidance on Cancer Services, 2010) Improving Outcomes for People with Skin Tumours Including Melanoma (update): the Management of Low-risk Basal Cell Carcinomas in the Community.
6. M. Venturini, G. Gualdi, A. Zanca, L. Lorenzi, G. Pellacani, and P. G. Calzavara-Pinton, "A new approach for presurgical margin assessment by reflectance confocal microscopy of basal cell carcinoma," Br. J. Dermatol. **174**, 380–385 (2016).
7. M. Nassiri-Kashani, B. Sadr, F. Fanian, K. Kamyab, P. Noormohammadpour, M. M. Shahshahani, H. Zartab, M. M. Naghizadeh, M. Sarraf-Yazdy, and A. Firooz, "Pre-operative assessment of basal cell carcinoma dimensions using high frequency ultrasonography and its correlation with histopathology," Skin ResEarch & Technology **19**, e132–e138 (2013).
8. I. Kopriva, A. Persin, N. Puizina-Ivic, and L. Miric, "Robust demarcation of basal cell carcinoma by dependent component analysis-based segmentation of multi-spectra fluorescence images," Photochem. Photobiol. B **100**, 10–18 (2010).
9. M. Balu, C. B. Zachary, R. M. Harris, T. B. Krasieva, K. Konig, B. J. Tromberg, and K. M. Kelly, "In vivo multiphoton microscopy of basal cell carcinoma," JAMA Dermatol. **151**, 1068–1074 (2015).
10. R. Patalay, C. Talbot, Y. Alexandrov, M. O. Lenz, S. Kumar, S. Warren, I. Munro, M. A. A. Neil, K. Konig, P. M. W. French, A. Chu, G. W. H. Stamp, and C. Dunsby, "Multiphoton multispectral fluorescence lifetime tomography for the evaluation of basal cell carcinomas," PLoS One **7**, e43460 (2012).
11. K. Busam, C. Charles, C. Lohmann, A. Marghoob, M. Goldgeier, and A. Halpern, "Detection of intraepidermal microscopy," Melanoma Res. **12**, 349–355 (2002).
12. M. A. Boone, M. Suppa, G. Pellacani, A. Marneffe, M. Miyamoto, I. Alarcon, C. Ruini, R. Hofmann-Wellenhof, J. Malvehy, G. B. Jemec, and V. Del Marmol, "High-definition optical coherence tomography algorithm for discrimination of basal cell carcinoma from clinical BCC imitators and differentiation between common subtypes," J. Eur. Acad. Dermatol. Venereol. **29**, 1771–1780 (2015).
13. M. A. L. M. Boone, S. Norrenberg, G. B. E. Jemec, and V. Del Marmol, "Imaging of basal cell carcinoma by high-definition optical coherence tomography: histomorphological correlation. A pilot study," Br. J. Dermatol. **167**, 856–864 (2012).
14. T. Maier, M. Braun-Falco, T. Hinz, M. H. Schmid-Wendtner, T. Ruzicka, and C. Berking, "Morphology of basal cell carcinoma in high definition optical coherence tomography: en-face and slice imaging mode, and comparison with histology," J. Eur. Acad. Dermatol. Venereol. **27**, e97–e104 (2013).
15. M. Ulrich, T. von Braunmuehl, H. Kurzen, T. Dirschka, C. Kellner, E. Sattler, C. Berking, J. Welzel, and U. Reinhold, "The sensitivity and specificity of optical coherence tomography for the assisted diagnosis of nonpigmented basal cell carcinoma: an observational study," Br. J. Dermatol. **173**, 428–435 (2015).
16. A. G. Podoleanu and A. Bradu, "Master-slave interferometry for parallel spectral domain interferometry sensing and versatile 3D optical coherence tomography," Opt. Express **21**, 19324–19338 (2013).
17. A. Bradu, M. Maria, and A. G. Podoleanu, "Demonstration of tolerance to dispersion of master/slave interferometry," Opt. Express **23**, 14148–14161 (2015).
18. J. Wang, A. Bradu, G. Dobre, and A. Podoleanu, "Full-field swept source master-slave optical coherence tomography," IEEE Photon. J. **7** (2015).
19. A. Bradu and A. G. Podoleanu, "Imaging the eye fundus with real-time en-face spectral domain optical coherence tomography," Biomed. Opt. Express **5**, 1233–1249 (2014).
20. B. R. Penmetsa, M. Khandwala, A. Bradu, M. Hughes, C. A. Jones, J. Schofield, and A. G. Podoleanu, "Imaging of basal cell carcinoma tissue using en-face OCT," Proc. SPIE **7139**, 71390J (2008).
21. M. Khandwala, B. R. Penmetsa, S. Dey, J. B. Schofield, C. A. Jones, and A. Podoleanu, "Imaging of periocular basal cell carcinoma using en face optical coherence tomography: a pilot study," BJO **1136**, 1–5 (2010).

22. M. R. N. Avanaki, A. Hojjatoleslami, M. Sira, J. Schofield, C. Jones, and A. G. Podoleanu, "Investigation of basal cell carcinoma using dynamic focus optical coherence tomography," Appl. Opt. **52**, 2116–2124 (2013).

23. J. K. Patel, S. Konda, O. A. Perez, S. Amini, G. Elgart, and B. Berman, "Newer technologies/techniques and tools in the diagnosis of melanoma," Eur. J. Dermatol. **18**, 617–631 (2008).

24. N. Iftimia, G. Peterson, E. W. Chang, G. Maguluri, W. Fox, and M. Rajadhyaksha, "Combined reflectance confocal microscopy-optical coherence tomography for delineation of basal cell carcinoma margins: an ex vivo study," J. Biomed. Opt. **21**, 016006 (2016).

25. M. Ulrich, L. Themstrup, N. Carvalho, M. Manfredi, C. Grana, S. Ciardo, R. Kastle, J. Holmes, R. Whitehead, G. B. E. Jemec, G. Pellacani, and J. Welzel, "Dynamic optical coherence tomography in dermatology," J. Dermatol. **232**, 298–311 (2016).

26. G. Li, J. K. Tietze, X. Tao, D. Kulichova, T. Ruzicka, C. Berking, and T. Maier, "High-definition optical coherence tomography in the diagnosis of basal cell carcinoma evaluated by an experienced versus in experienced investigator," J. Clin. Exp. Dermatol. Res. **5**, 1000227 (2014).

27. A. Hojjatoleslami and M. R. N. Avanaki, "OCT skin imaging enhancement through attenuation compensation," Appl. Opt. **51**, 4927–4935 (2012).

28. A. Bradu, K. Kapinchev, F. Barnes, and A. Podoleanu, "Master slave en-face OCT/SLO," Biomed. Opt. Express **6**, 3655–3669 (2015).

29. A. Bradu, K. Kapinchev, F. Barnes, and A. Podoleanu, "On the possibility of producing true real-time retinal cross-sectional images using a graphics processing unit enhanced master-slave optical coherence tomography system," J. Biomed. Opt. **20** (2015).

30. M. A. Boone, M. Suppa, G. Pellacani, A. Marneffe, M. Miyamoo, I. Alarcon, C. Ruini, R. Hofmann-Wellenhof, J. Malvehy, G. B. Jemec, and V. Del Marmol, "High-definition optical coherence tomography algorithm for discrimination of basal cell carcinoma from clinical BCC imitators and differentiation between common subtypes," J. Eur. Acad. Dermatol. Venereol. **29**, 1771–1780 (2015).

31. T. Gambichler, I. Plura, P. Kampilafkos, K. Valavanis, M. Sand, F. G. Bechara, and M. Stucker, "Histopathological correlates of basal cell carcinoma in the slice and en face imaging modes of high-definition optical coherence tomography," Br. J. Dermatol. **170**, 1358–1361 (2014).

32. A. J. Coleman, T. J. Richardson, and G. Orchard, et al., "Histological correlates of optical coherence tomography in non-melanoma skin cancer," Skin Research & Technology **19**, e10–e19 (2013).

33. M. A. Boone, S. Norrenberg, G. B. Jemec, and V. Del Marmol, "Imaging of basal cell carcinoma by high-definition optical coherence tomography: histomorphological correlation. A pilot study," Br. J. Dermatol. **167**, 856–864 (2012).

34. S. A. Hojjatoleslami, M. R. N. Avanaki, and A. G. Podoleanu, "Image quality improvement in optical coherence tomography using Lucy-Richardson deconvolution algorithm," Appl. Opt. **52**, 5663–5670 (2013).

35. M. R. N. Avanaki, R. Cernat, P. J. Tadrous, T. Tatla, A. G. Podoleanu, and S. A. Hojjatoleslami, "Spatial compounding algorithm for speckle reduction of dynamic focus OCT images," IEEE Photon. Technol. Lett. **25**, 1439–1442 (2013).

36. M. Mogensen, T. Joergensen, L. Thrane, B. M. Nurnberg, and G. B. E. Jemec, "Improved quality of optical coherence tomography imaging of basal cell carcinomas using speckle reduction," Exp. Dermatol. **19**, e293–e295 (2009).

37. M. Maria, M. J. M. Marques, C. Costa, A. Bradu, T. Feuchter, L. Leick, and A. G. H. Podoleanu, "Broadband master-slave interferometry using a super-continuum source," Proc. SPIE **9697**, 96972R (2016).

38. M. Mogensen, T. M. Joergensen, B. M. Nurnberg, H. A. Morsy, J. B. Thomsen, L. Thrane, and G. B. Jemec, "Assessment of optical coherence tomography imaging in the diagnosis of non-melanoma skin cancer and benign lesions versus normal skin: observer-blinded evaluation by dermatologiss and pathologists," Dermatol. Surg. **35**, 965–972 (2009).

39. J. M. Olmedo, K. E. Warschaw, J. M. Schmitt, and D. L. Swanson, "Optical coherence tomography for the characterization of basal cell carcinoma in vivo: a pilot study," J. Am. Acad. Dermatol. **55**, 408–412 (2006).

# Queries

1. AU: Edit to title OK?

2. AU: The ref [27 and 36] is not cited in the article.

3. AU: The funding information for this article has been generated using the information you provided to OSA at the time of article submission. Please check it carefully. If any information needs to be corrected or added, please provide the full name of the funding organization/institution as provided in the CrossRef Open Funder Registry (http://www.crossref.org/fundingdata/registry.html).

4. AU: Please provide us the complete details for Ref. [5].

5. AU: Please note Ref. 12 and 30 are the same, suggest which reference to be removed. Also note that 27 and 36 are not cited in text, please provide suitable citation in text. All references must be cited in sequential order.

6. AU: Please provide page range.

7. AU: Please provide page range.

8. AU: Please write out all author names instead of using et al. in Ref. 32.

9. Please provide complete author names for Ref. [29].